1 **Simulating the variations of carbon dioxide in the global atmosphere**

2 **on the hexagonal grid of DYNAMICO coupled with the LMDZ6 model**

4 Zoé Lloret[1], Frédéric Chevallier[1], Anne Cozic[1], Marine Remaud[1*], Yann Meurdesoif[1]

5 [1]Laboratoire des Sciences du Climat et de l'Environnement, LSCE/IPSL, CEA-CNRS-UVSQ, Université Paris-Saclay, Gif-sur-
6 Yvette, France

7 [*] currently at Faculty of Science, A-LIFE, Vrije Universiteit Amsterdam, 1081 HV Amsterdam, the Netherlands

8 *Correspondence to*: Zoé Lloret (zoe.lloret@lsce.ipsl.fr)

9 **Abstract.** Efforts to monitor the emissions and absorptions of atmospheric carbon dioxide (CO_2) over the globe and to
10 understand their varying regional patterns with greater accuracy have intensified in recent years. This study evaluates the
11 performance of a new model coupling, ICO, built around the Laboratoire de Météorologie Dynamique atmospheric general
12 circulation model (LMDZ) for simulating CO_2 transport. ICO utilizes the new icosahedral hydrostatic dynamical core called
13 Dynamico running on an unstructured grid, which enables potential improvements in spatial resolution at the Equator while
14 removing artificial distortions and numerical filters at the poles. Comparisons with a reference configuration using a structured
15 latitude-longitude grid reveal that ICO well captures seasonal variations in CO_2 concentrations at surface stations. While not
16 significantly enhancing the capture of complex seasonal patterns, ICO maintains comparable accuracy. Both configurations
17 exhibit similar vertical CO_2 concentration profiles and display a consistent bias in the lower stratosphere relative to observational
18 data. ICO demonstrates advantages in computational efficiency and storage, thanks to its reduced cell count per level and a
19 homogeneous grid structure. It holds promise for future developments, including with the LMDZ offline model and associated
20 inversion system, which contribute to the Copernicus Atmosphere Monitoring Service. Overall, the ICO configuration showcases
21 the efficacy of utilizing an unstructured grid for the physics, and the capability of Dynamico in accurately simulating CO_2
22 transport. This study emphasizes the importance of advanced modeling approaches and high-resolution innovative grids in
23 enhancing our understanding of the global carbon cycle and refining climate models.

24 **1 Introduction**

25 The key role of carbon dioxide (CO_2) in climate change has motivated increasing efforts in recent decades to monitor its
26 variations in the global atmosphere. Sources and sinks of this trace gas are found primarily on the Earth's surface. They induce
27 the highest CO_2 gradients in the boundary layer, for example around anthropogenic emission hotspots, while their direct
28 influences gradually mix over time at all altitudes to contribute to the overall CO_2 background. The distribution of CO_2 in the
29 atmosphere therefore spans a wide range of spatial and temporal scales, mainly combining influences from surface sources,
30 surface sinks and meteorology. This complexity is sampled by growing high-quality observation networks on the ground, in the
31 atmosphere (aircraft, balloons, drones) and in space (e.g., Ciais et al., 2014; Crisp et al., 2018). It is also simulated, more or less
32 well, by Atmospheric General Circulation Models (GCMs) and dedicated tracer transport models (e.g., Remaud et al., 2018;
33 Basu et al., 2018; Agustì-Panareda et al., 2022). Many uncertainties in the model input data (boundary conditions, meteorology)
34 and the model equations (advection schemes, subgrid parameterizations) still limit these simulations. However, there is a strong
35 incentive towards higher spatial resolutions in order to benefit from an increased realism for orography, coastlines, and known
36 emission or absorption hot-spots, and to reduce any artificial smoothing of the 3D fields (Agustì-Panareda et al., 2019).

37   However, this wish is tempered by the need to carry out long simulations of this long-lived tracer, typically several years, that

38   may be massively repeated in the case of inverse modeling. Increasing the resolution without affecting the time-to-solution leads

39   to revisiting the numerical efficiency of models in order to gain computing time margins. Porting codes on Graphical Processing

40   Units (GPUs) may largely contribute to this effort (Chevallier et al., 2023), but not enough to close the gap with, e.g., the

41   kilometric resolution of the current space-borne observations. In particular, models running on a regular longitude-latitude grid

42   face scaling limitations due to advection at the poles requiring significant data communication to solve the problem of resolution

43   clustering. This data exchange can create a computing bottleneck on supercomputers using large amounts of processors

44   (Staniforth & Thuburn, 2012). In this paper, we are addressing this specific issue for the simulation of CO_2 using an unstructured

45   quasi-uniform grid made of non-quadrilateral grid cells. Such a solution has been explored by few models so far, either for use in

46   Earth system models or directly for atmospheric inversion (Niwa et al., 2017; Giorgetta et al., 2018; Sakaguchi et al., 2020).

47   We build on the dynamical core Dynamico (Dubos et al., 2015), which has recently been integrated into LMDZ which is the

48   GCM (Hourdin et al., 2020) of the Laboratoire de Météorologie Dynamique. LMDZ has been used as the atmospheric

49   component of the Institut Pierre-Simon-Laplace (IPSL) Earth system model (Sepulchre et al., 2020) and for the Climate Model

50   Intercomparison Project (CMIP) with its traditional regular longitude-latitude grid. For comparisons with real observations, e.g.,

51   for inverse modeling, it is nudged to horizontal wind fields obtained from a numerical weather forecast reanalysis.

52   This paper evaluates the ability of this new coupling of the LMDZ GCM using the Dynamico dynamical core to transport a long-

53   lived tracer like CO_2. Dynamico has been extensively compared to other dynamical cores (Ullrich et al., 2017), but the same has

54   not been done yet for its coupled configurations. Coupling it to the LMDZ GCM also represents the first step towards the use of

55   Dynamico for inverse modeling. We compare it to the previous equivalent version running on a regular longitude-latitude grid

56   and to various observations of CO_2 mole fractions over a 40-year period.

57   Section 2 describes the two configurations of our GCM, the experiments we ran to compare them, and the method for our study.

58   Section 3 presents the results of the direct comparison between our models and the observations. Section 4 concludes the study.

2 Presentation of the model and experiments

2.1 Model description

2.1.1 LMDZORINCA - Regular longitude-latitude configuration

62   Our general circulation model configuration consists of the coupling between the LMDZ model of Hourdin et al. (2013, 2020)

63   itself, an aerosol and reactive chemistry model called INteractions between Chemistry and Aerosols (INCA, Hauglustaine, et al.,

64   2004) and the Organizing Carbon and Hydrology in Dynamic Ecosystems land surface model (ORCHIDEE, Krinner et al.,

65   2005). ORCHIDEE simulates the water and energy exchanges between the soil and the atmosphere, but yearly land cover maps

66   were used here instead of simulating vegetation dynamics. In the following, we will refer to this LMDZ-INCA-ORCHIDEE

67   coupled model on the regular latitude-longitude grid as REG for simplicity.

68   Tracers, such as CO_2, are modeled by INCA, and their transport is calculated and synced with the LMDZ GCM physics timestep

69   every 15 minutes. Chemical processes are also calculated every 15 minutes by computing differential equations to update the

70   atmospheric concentration fields of each cell. Using tracers from INCA instead of only having them in LMDZ allows interaction

71   between chemical reactions and the tracer transport process, which is crucial for some tracers such as CH_4, although it has no

72   impact on CO_2.

73 The latest version of LMDZ physics is described in Hourdin et al. (2020). Most notably for tracer transport, dry and cloudy

74 shallow convection is separated from deep convection. Shallow convection is unified and combines the Mellor and Yamada

75 (1974) diffusive approach for small-scale turbulence with a thermal plume model (Rio & Hourdin, 2008) for the boundary layer.

76 Deep convection uses a modified version of the mass-flux formulation of Emanuel (1991) (Grandpeix et al., 2004, Rochetin et

77 al., 2014). Longwave radiation is modeled using the Rapid Radiation Transfer Model (RRTM; Mlawer et al., 1997), and

78 shortwave radiation uses a 6-band code derived from Fouquart and Bonnel (1980).

79 The dynamical core of LMDZ is a mix of a finite difference and finite volume discretization on the sphere of the primitive

80 equations of meteorology and of transport equations (Hourdin et al., 2006, 2013). Water and other tracers are advected with a

81 scheme from Van Leer (1997), and angular momentum is conserved numerically. This full configuration was previously

82 evaluated for CO_2 transport by Remaud et al. (2018).

83 The dynamical core of LMDZ is parallelized in latitude using distributed memory with the Message Passing Interface standard

84 (MPI) and in the vertical with shared memory using the Open Multi-Processing interface (OpenMP). A longitudinal filter near

85 the poles avoids the use of very small time steps, but limits the efficiency of any parallelism along the longitudes.

86 The parallelization of the physical parameterizations within LMDZ follows a different approach. It utilizes a combination of MPI

87 and OpenMP processes with shared memory by splitting a single vector that runs through the entire horizontal grid into

88 independent domains. This is possible due to the fundamental 1-D nature of the LMDZ physical parameterizations that only

89 compute vertical transfers. The performance of the model is optimized by using domain decomposition parallelism on the

90 horizontal layer with MPI and shared memory parallelism with OpenMP. For LMDZ at our resolution, the optimal compromise

91 between resources and performance is achieved by using 71 MPI processes with 8 OpenMP threads running on 568 cores

92 (Hourdin, 2020).

93 **2.1.2 ICOLMDZORINCA - unstructured grid configuration**

94 ICOLMDZORINCA is a novel configuration of our coupled model that integrates the previously described ORCHIDEE land

95 surface model, the INCA chemistry model, and the physics module of the LMDZ model. The previous dynamical core in LMDZ

96 has been replaced by a new one, known as DYNAMICO (Dubos et al., 2015), which operates on a quasi-uniform icosahedral C-

97 grid for its horizontal mesh. In the following, we will refer to this DYNAMICO-LMDZ-INCA-ORCHIDEE coupled model as

98 ICO for simplicity.

99 The hydrostatic and shallow-atmosphere non-hydrostatic Euler equations can be solved using the DYNAMICO dynamical core

100 (Ullrich et al., 2017). The mesh is based on a tessellation of the sphere into triangles, which when joined, creates the primal

101 hexagonal-pentagonal mesh. A quasi-uniform grid avoids any singularity at the poles, thereby improving the load balancing on

102 parallel computers. By construction, this grid has a coarser resolution than a regular longitude-latitude grid in the high latitudes,

103 even when accounting for the polar filter (Herrington et al., preprint). Figure 1 provides an example of a visual representation of

104 the icosahedral C-grid.

105 Kinematics and dynamics were separated as much as possible so that transport equations do not use any information from the

106 momentum equations. The kinematics handle the transport of mass, potential temperatures, and tracers using the mass fluxes

107 computed by the dynamics. The vertical transport uses a slope-limited Van Leer's scheme (Van Leer, 1977) and does not differ

108   from the vertical transport of LMDZ. The fully discrete finite volume horizontal advection scheme is described in Dubey et al.
109   (2015). It uses a flux-corrected transport approach to stay positive-definite rather than slope limiters.

110   To achieve efficient parallelism in the horizontal dimension, the ICO configuration partitions the mesh into rhombi, whose sides
111   pass through the centers of some of the hexagons. The hexagons covered by a rhombus are processed together and the rhombi
112   can be processed in parallel. This parallelization strategy is implemented with a combination of OpenMP and MPI.

113   The vertical parallelization is identical to the one in the REG configuration.

114
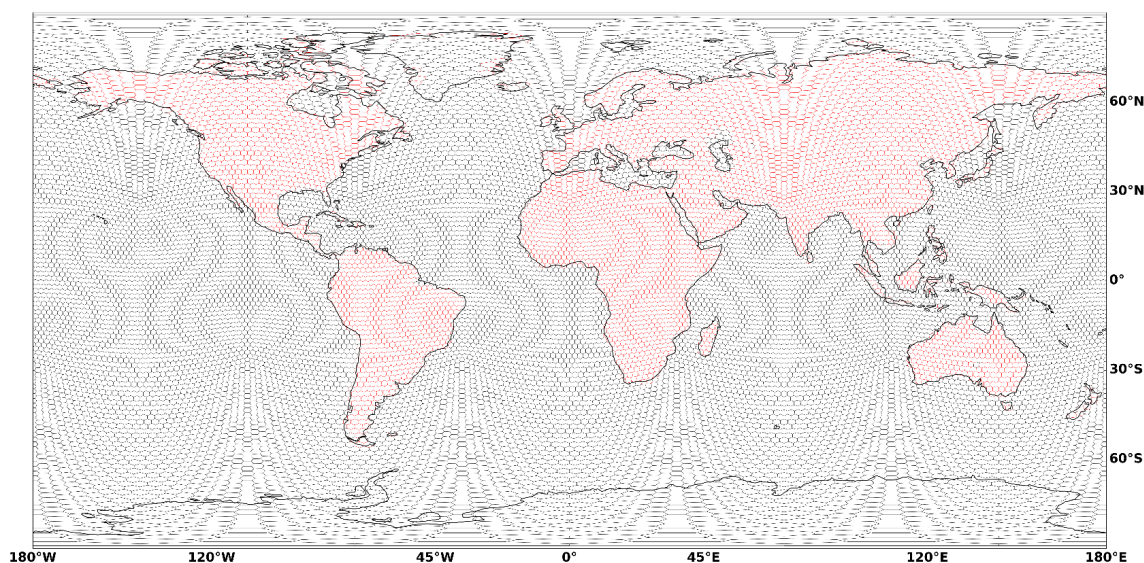
115
116
117   **Figure 1: Unstructured grid of the ICO configuration used here.**

118   **2.2 Description of the simulations**

119   For each configuration (REG and ICO), we have run a simulation from 1979 to 2020. The first year is used for spin-up and is not
120   analyzed. In both configurations, the model was not let free, but its large-scale atmospheric circulation was kept in the vicinity of
121   the observed one by nudging its 6-hourly horizontal winds toward the ERA5 reanalysis (Hersbach et al., 2020) with a relaxation
122   time of 3 hours. The nudging drives the large-scale atmospheric circulation of the model. Initial atmospheric CO_2 mixing ratios
123   values were set using the Copernicus Atmosphere Monitoring Service (CAMS) atmospheric inversion, version 20r2 (Chevallier
124   et al., 2005; https://atmosphere.copernicus.eu/, access 31 May 2023). This same product prescribed the CO_2 surface fluxes every
125   3 hours. These surface fluxes carry some imprint from the REG model with a regular grid since CAMS uses an older REG model
126   version at coarser spatial resolution. Still, after Remaud et al. (2018) who tested a distinct set of surface fluxes for their model
127   evaluation within a similar framework, we consider that this imprint hardly affects our conclusions.

128   The boundary files used for the two simulations were identical. However, for the simulation running on ICO, the boundary files
129   were either interpolated or recreated onto the new grid ahead of time to fit the unstructured grid or interpolated during execution.

130 The initial total mass of CO_2 in the atmosphere had a difference of only 0.01% between the two simulations because of these
131 operations.

132 We had an hourly model output for all variables. This high frequency output was chosen in order to well assess the differences
133 in synoptic variability of tracer transport between our two model configurations.

134 We ran REG on a horizontal grid of 144 points in longitude × 143 grid points in latitude, which corresponds to a resolution of
135 2.5° in longitude and 1.27° in latitude, equivalent to 278 km by 140 km at the equator. We use 79 vertical layers going up to 80
136 km in altitude, with around 25 layers dedicated to the first 2 km. The complete grid configuration is described in more detail in
137 Hourdin et al. (2020).

138 We ran ICO on a horizontal grid of 16002 cells, and the same 79 vertical layers. This gives an horizontal resolution at the equator
139 of around 2.5° in longitude and 1.25° in latitude, each cell has the area of an hexagon of side 110 km in order to have similar
140 resolution at the equator to the equivalent longitude-latitude grid from REG. With this setup, ICO has 22% less cells than REG.

141 **2.3 Observational data**

142 To compare our simulated tracer concentrations to observations, we sampled the concentration fields at the nearest cell center,
143 model level and timestamp for each data point. We used the high-quality measurements of the CO_2 GLOBALVIEWplus
144 v8.0_2022-08-27 ObsPack database (Schuldt et al., 2022).

145 In this dataset, observations were calibrated according to the WMO CO_2 X2019 scale (Hall et al., 2021). Like for inverse
146 modeling with LMDZ (Chevallier et al., 2010), only afternoon non flagged data from 12:00 to 16:00 local time were selected for
147 continuous in-situ surface stations under 1000 m above sea level (a.s.l.), and only night time data from 00:00 to 4:00 local time
148 were kept for in-situ stations above 1000 m a.s.l. All flask data, and all upper-air data (aircraft data and AirCore measurements)
149 were kept. This selection accounts for the usual failure of transport models to well represent the accumulation of tracers at low
150 altitude during the night as well as the inability to model the phenomenon in mountain stations where air masses are advected
151 during daytime through updrafts on the sun-exposed slopes (Geels et al., 2007).

152 We divided the observations into three groups: surface in situ and flask data, aircraft observations and observations from AirCore
153 flights. We used the aircraft measurements and AirCore data to obtain vertical profiles of CO_2 concentration. AirCore (Karion et
154 al. 2010) is an atmospheric sampling system consisting of an open ended steel tube launched from an aerial platform and that
155 collects many successive samples of the ambient air when descending. For surface data, 107 stations have been selected from the
156 Obspack dataset out of the original 222 stations. Surface stations with less than 5000 measurement points that passed the initial
157 data selection described above over the entire duration of the study were excluded from the analysis. For aircrafts, we have
158 selected 33 sites and campaigns out of a possible 51, only keeping those with more than 2000 measurement points. For the
159 AirCore data, we kept all observations. The full list of sites and datasets used is presented in Table 1 and Table 2 as a
160 supplement.

161 The uncertainty of the reference CO_2 mixing ratio measurements used here is on the order of 0.1 ppm (see, e.g., Crotwell et al.,
162 2020, for the systematic errors and Hazan et al., 2016, for the standard deviation). It is negligible compared to the model
163 uncertainty due to transport error which is on the order of 1 ppm under 3000 m (Lauvaux et al., 2009) and is not further
164 discussed in the following. Collection altitude determination error from AirCore measurements can be high and depends on the

altitude, and is on the order of 250 m below 20 km and up to 1 km above that altitude (Wagenhäuser et al., 2021). We discuss the potential impact of these uncertainties on our model evaluation in section 3.5.2.

2.4 Evaluation methodology

2.4.1 Surface stations

For surface stations with continuous measurements, we used a curve-fitting method on both the model and observations CO_2 mixing ratios time series to extract the annual mean, the seasonal cycles and the synoptic variations. A smoothed function consisting of a second-order polynomial and eight harmonics was used to fit the time series over the 19080-2020 period. The polynomials were used to calculate the annual trend and growth rate, while the harmonics were used to get the seasonal cycle. The synoptic variations are obtained from the difference between the raw data and the fitted smooth curve.

To evaluate the two model configurations performance between each other and compared to observations we use metrics which we will describe in the following subsections.

2.4.2 Annual gradient between stations

We use the measurements from South Pole station (SPO), which is far from any major CO_2 source or sink, to validate the simulated background growth rate of CO_2 concentrations. Then, we study the cross-site gradients by calculating the yearly growth rate at each site relative to SPO. To do so, we average the annual growth rate of the CO_2 concentration over the 1980-2020 period for each site and subtract the value at SPO. Comparing the observed and modeled values of this variable informs us on both the growth rate of the CO_2 concentration at each site, and on concentration gradients of our transport model which are key for use in an inverse system. To study the interannual variation of these growth rates, we calculate their standard deviation for both measurements and models. We normalize the average model's standard deviation by dividing it by the measurement standard deviation. This gives us information on how well the model captures the magnitude and direction of these variations.

We compute the yearly growth rate for each year of the 1980-2020 period using the smooth curved fit described above, before averaging it. To evaluate this variable, we then look at the mean bias and the root-mean-square error (RMSE) of the CO_2 concentration gradient for each station relative to SPO.

2.4.3 Seasonal cycle

We evaluate the capacity of our model to represent the CO_2 seasonal cycle by comparing the phase and amplitude of the harmonics of their smoothed fitted curve to the one of the measurements at each station. At each measurement site we calculated the Pearson correlation coefficient between measurements and model time series to evaluate the phase of the seasonal cycle. And we evaluated the amplitude of the seasonal cycle by looking at the ratio between peak-to-peak amplitudes of the harmonics. We normalized this variable by dividing the values of the model's seasonal cycle peak-to-peak amplitude at each station by the ones from the observations.

2.4.4 Synoptic variability

To evaluate our model ability to represent the phase of the CO_2 synoptic variability we again used the Pearson correlation coefficient between the residual from the smoothed fitted curve of the model and the measurements. The amplitude of the synoptic variations at each station were evaluated by the normalized standard deviation.

199 **2.4.5 ERA5**

200 To compare the simulated temperature with the ERA5 reanalysis, we divided the output into seasons and then into bins of 30°

201 latitudes. For each bin, we averaged the data for each model level for each season. We then did an identical operation on the

202 ERA5 reanalysis data before comparing the two.

203 **2.4.6 Aircraft measurements**

204 The aircraft measurements have been binned into 1 km altitude bins, and then averaged for each hour and over each bin for each

205 site or campaign. Then the data was averaged over all sites and campaigns. This process was done for each season and for the

206 whole year.

207 **2.4.7 AirCore measurements**

208 For measurements from AirCore, we binned and averaged the data into 50 altitude bins, from the ground to the maximum

209 altitude of the data (27 km) to get an average vertical profile of CO_2 concentrations.

210 **3 Results and discussions**

211 **3.1 Mass conservation**

212 Conservation of mass is closely examined for the simulation of long-lived tracers as it directly supports the simulation of the

213 tracer's global growth rate. In inverse systems, it makes it possible to infer surface fluxes far from observations, far in space as

214 well as in time. In practice, numerical approximations may make the model lose or gain tracer mass (Houweling et al., 2010).

215 In this section, we evaluate mass conservation in our models by calculating the total mass of CO_2 at the beginning and at the end

216 of the simulations. To do that, we multiply the CO_2 mole fraction with the air mass in each cell and sum it over the whole globe.

217 We then compare the difference between the CO_2 mass at the end and beginning with the total amount of prescribed surface CO_2

218 fluxes. The difference between these two values is the amount of CO_2 lost or gained by our model over time.

219 $$\Delta M_{CO_2} = M^e_{CO_2} - M^i_{CO_2} = \sum_{n=1}^{N\,cell} m^{n,e}_{air} \times c^{n,e}_{CO_2} - \sum_{n=1}^{N\,cell} m^{n,i}_{air} \times c^{n,i}_{CO_2} \ (1)$$

220 $$M^{emi}_{CO_2} = \sum_{t=1,n=1}^{T,N} emi^{t,n}_{CO_2} \times area \ (2)$$

221 $$M_{loss} = M^{emi}_{CO_2} - \Delta M_{CO_2} \ (3)$$

222 For REG, the difference is equal to -0.13 % of the CO_2 mass emitted over the 1979 - 2020 period. For ICO it is -0.28 % for this

223 same period.

224 Therefore, while our models do not exactly conserve mass, they lose only around 0.014 GtC integrated over 10 years for REG,

225 and 0.027 GtC for ICO.

226 The total amount of CO_2 in each model also depends on the prescribed surface CO_2 fluxes described in section 2.2 ($M^{emi}_{CO_2}$)

227 which are interpolated on the 2 different grids and therefore, not strictly identical either for each configuration. However, the

228 average difference in yearly emitted CO_2 between the two model configurations is 0.0006 % only.

3.2 Computational efficiency

Simulations were run on the Skylake partition of the Joliot Curie, a BullSequana X1000 supercomputer operated since 2017 by Très Grand Centre de Calcul (TGCC, Bruyère-le-Châtel, France). This partition is composed of 1656 nodes, each of which has an Intel Skylake 8168 dual-processor. We used the Intel Fortran compiler version 20.0.0.

For our simulations REG used 47 MPI processes and 8 OpenMP threads for a total of 384 CPU cores, while ICO employed 80 MPI processes and 4 OpenMP threads for a total of 336 CPU cores. On average, over the whole simulation, REG achieved a wall-clock-time of 2594 seconds and consumed 2767 CPU hours per month simulated, while ICO executed in 2238 seconds and consumed 2089 CPU hours per month simulated. These results indicate that ICO provides a speedup of 14% in total CPU hours consumed over REG, with 22% less cells.

These results are highly dependent on the given output frequency of our simulation, in our case outputting large amounts of variables every hour greatly increases the execution time and becomes a computational bottleneck.

To better compare the configurations scaled up and in their ideal state, speed tests were run with identical numbers of CPUs: 71 MPI processes and 8 OpenMP threads with an additional 8 CPU used for XIOS servers for a total of 576 CPU cores. XIOS is a tool used for reading the input files in parallel and we chose 8 servers to ensure that this operation does not become a computational bottleneck for our models. Only monitoring files tracking the progress of the simulations were output, no physical variables were saved in order to avoid comparing the time it takes to write the files on disk. To avoid variability due to individual node performance, the tests were performed multiple times over several days, and outlier months caused by node performance issues were removed.

The average monthly time to completion in this setup for REG was 823 seconds (132 CPU hours), and for ICO 662 seconds (106 total CPU hours). This shows that for identical computational setups, ICO is on average 20% faster than REG.

This speedup is comparable to the reduced number of cells in ICO. For our spatial resolution, it seems that other differences such as the absence of a polar filter for ICO did not significantly improve the computational speed.

3.3 Vertical temperature profiles

To get a first idea of the differences between REG and ICO simulations, we consider atmospheric temperature and compare it with ERA5 values. Note that our models are nudged toward ERA5 horizontal winds (Section 2.2), but do not use the ERA5 temperature fields. Figure 2 shows the vertical profiles of the average temperature over the year 2000 for different zonal cuts in 60° latitude increments. We can already see that REG and ICO differ on several aspects for different altitudes. The tropopause height, as identified by the change in the vertical temperature gradient, is the same in both configurations, but its temperature varies between 2.5 K to 5 K for each configuration outside of the tropics. At the stratopause, a difference of up to 10 K for the yearly temperature average in high latitudes is observed between the simulations from REG and ICO (Not shown on the figure).
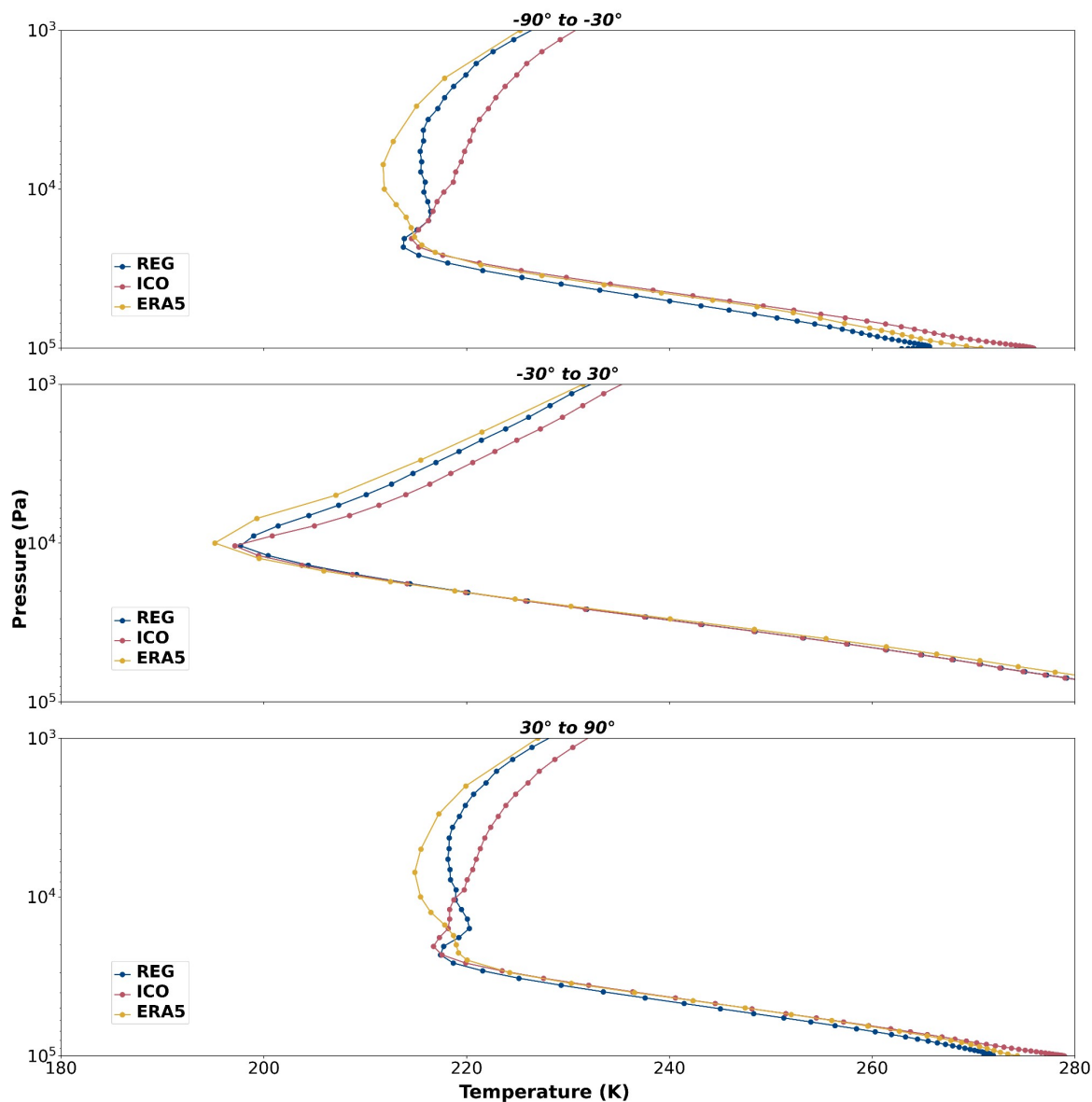
Figure 2: Vertical profile of zonal temperatures averaged over the year 2000 for the two model configurations and the ERA5 reanalysis, with REG in blue, ICO in red and ERA5 in yellow.

Looking at the temporal change of the temperature rather than yearly averages reveals a different pattern. We can see on Fig. 3 that the large temperature difference at the stratopause between our configurations is only present during winters for high latitudes. During summers, both configurations have much more similar temperatures in these latitudes, and all year around in the tropics. This is explained by the fact that during summers, the polar stratopause is mainly driven by ozone, whereas in winter it is driven by gravity-waves (Hitchman et al., 1989). The difference in parametrization and tuning of gravity waves in DYNAMICO used in our new configuration ICO compared to the previously used and much-tested REG version likely explains the observed differences in temperature of the stratopause. This large difference in temperature in the stratosphere also affects temperature lower in the troposphere, as has been shown for the stratospheric dynamics of the LMDZ GCM in Lott et al. (2005).

270 Future versions of the ICO configuration will contain a better parametrization of gravity waves as well as the introduction of a

271 so-called "sponge layer" (Shepherd et al., 1996) to nudge high atmospheric winds towards zonal averages, which was already

272 present in the REG configuration but not in ICO yet.

273
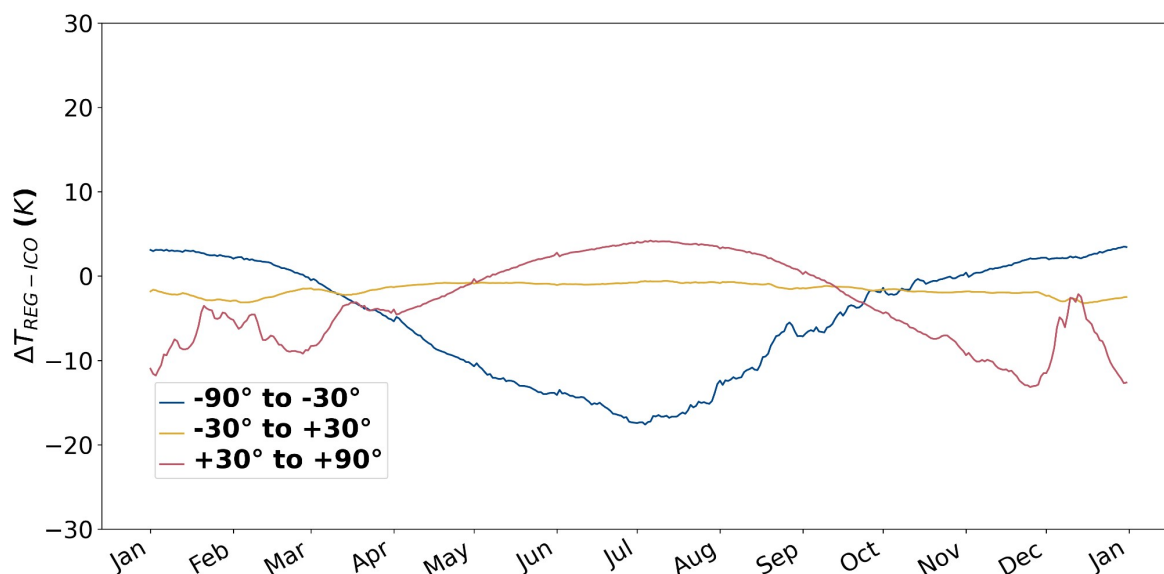
Figure 3: Time series of the average difference in zonal temperature at the stratopause (53 km) between the two model configurations REG and ICO for the year 2000, divided in 3 latitude zones of 60°.

276 We now turn to CO_2 concentrations to see how the different models affect tracer transport.

277 3.4 Seasonal analysis

278 3.4.1 Annual gradient

279
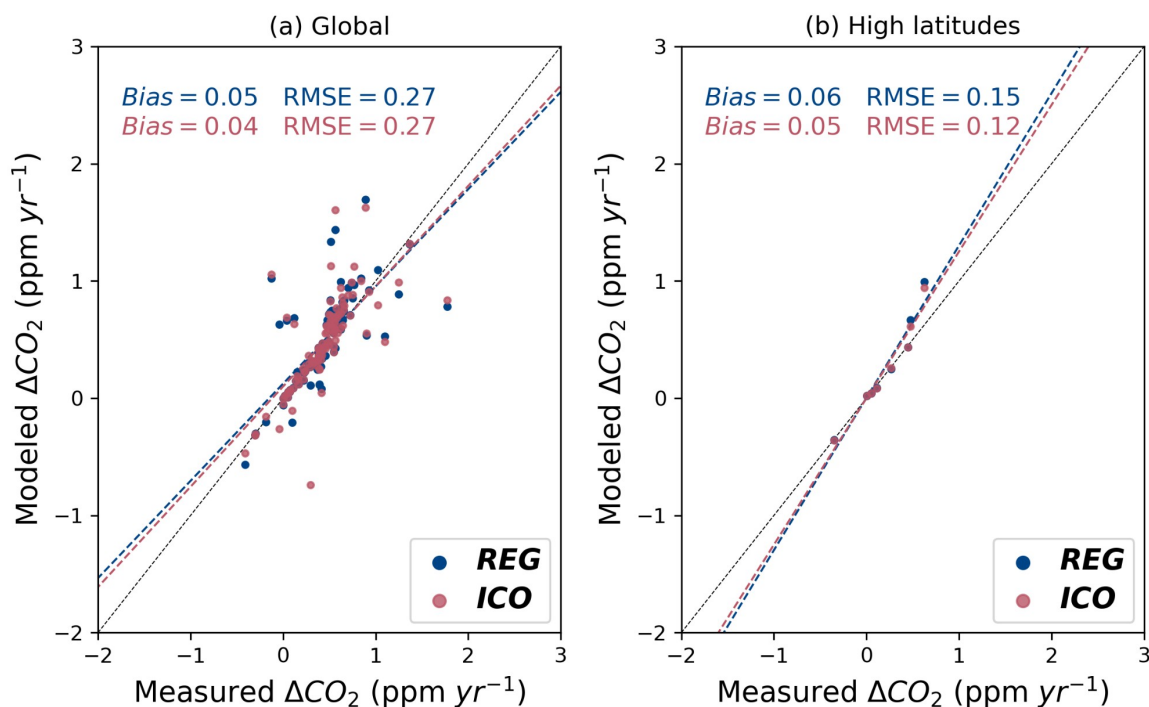
Figure 4: Annual gradients of CO$_2$ mixing ratio compared to SPO averaged over the 1980-2020 period for every station (a) or only stations at high latitudes (> 70°N/S) (b). Blue circles are the model outputs for the REG configuration, and red circles for the ICO configuration. The dotted lines correspond to the linear fitted lines of the corresponding colored configurations, and the black dotted lines correspond to the 1:1 relation.

284 Figure 4 shows the annual gradients of surface stations compared to SPO averaged over the 1980-2020 period, and for the two

285 model configurations the differences between the modeled and observed values of this gradient. We find an average yearly

286 growth rate of CO$_2$ mixing ratio at SPO of 1.79 ppm per year from observations, and of 1.74 ppm per year for both the REG and

287 ICO configurations. This difference of 0.05 ppm between our models and observations shows that the background growth rate of

288 CO$_2$ concentration is well modeled and within the small uncertainty range of the observations.

289 When looking at all surface stations (a), the ICO configuration exhibits a slightly lower overall bias, but an identical spread as

290 seen by the root mean square error (RMSE). Both configurations show a positive bias of less than 0.1 ppm per year compared to

291 observations. The two model configurations therefore successfully model the annual gradients between surface stations over the

292 globe.
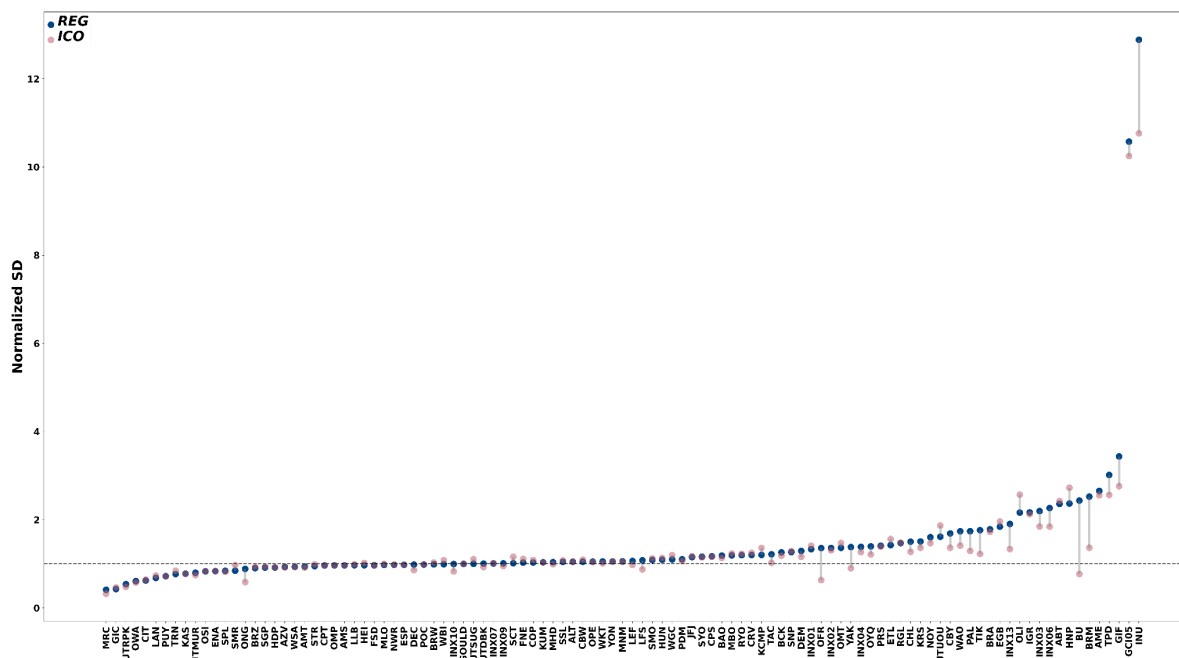
Figure 5: Normalized standard deviation of the annual gradient for both configurations for each station. Blue circles are the model outputs for the REG configuration, and red circles for the ICO configuration. The dotted line corresponds to the ideal normalized standard deviation of 1.

The average normalized standard deviation of the interannual variation in the annual gradient for the REG configuration is 1.43 and 1.3 for the ICO configuration. ICO therefore better captures the temporal variations of this gradient, but both configurations show a good agreement in magnitude of these variations for the majority of stations.

Since the biggest change regarding the grid and resolution takes place at the poles, we also checked the statistics and linear fit of these gradients restricted to stations at high latitudes (higher than 70°N and lower than 70°S). ICO performs just as well as REG for these stations in terms of both general bias and spread (Fig. 4 (b)). Even though the effective resolution is much coarser for the ICO configuration at these latitudes, it has not significantly affected the simulation of long term trends of CO_2 concentrations. This shows that forced resolution clustering at the poles of the regular latitude-longitude grid is not necessary for properly resolving tracer transport.

3.4.2 Seasonal cycle
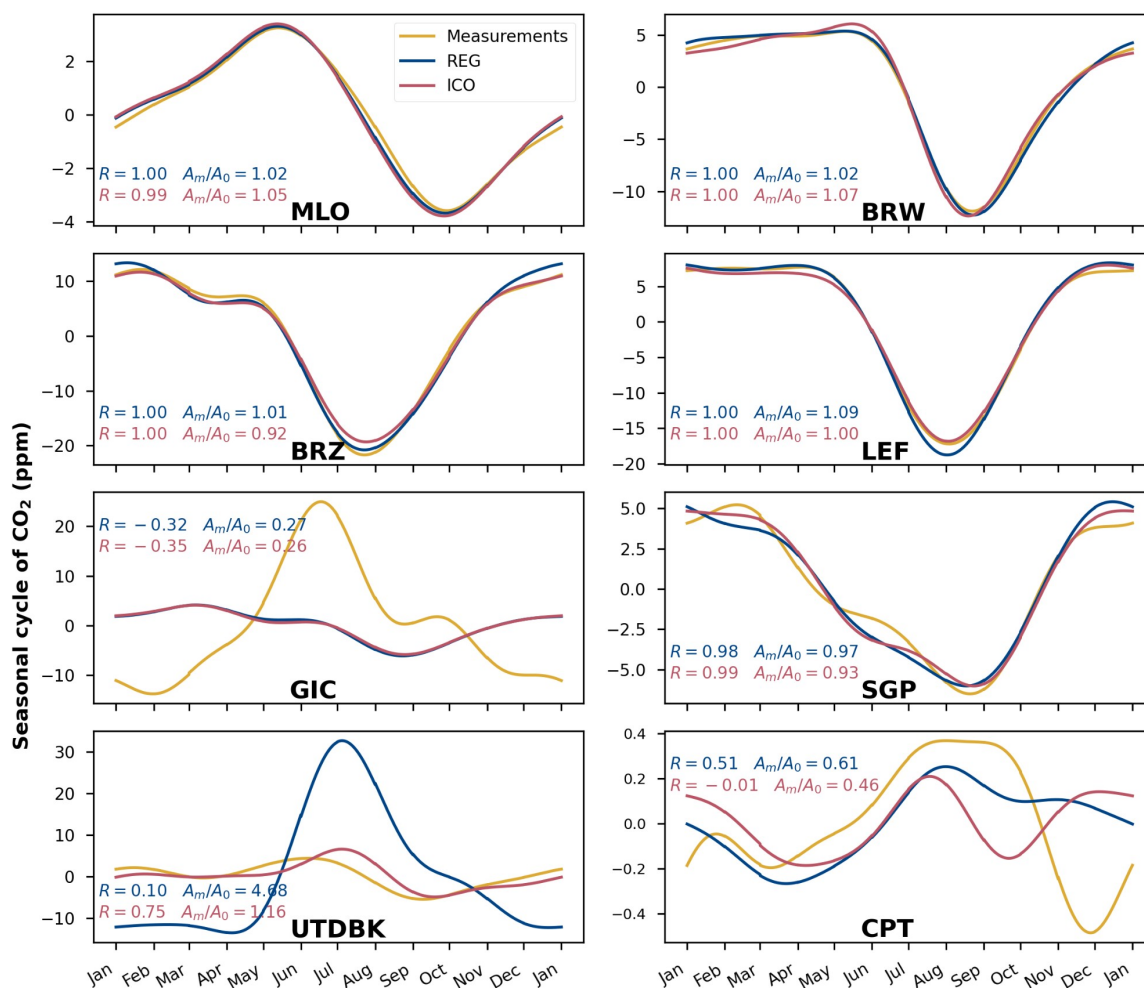
Figure 6: Seasonal cycle of the CO2 mixing ratio averaged over the period 1980-2020, in ppm, at a selection of surface stations for measurements, REG configuration and ICO configuration in yellow, blue and red respectively. The correlation coefficient and the peak-to-peak amplitude between the two model's output and measurements are displayed for each station. The selected stations were chosen to exemplify diverse behaviors: where both configurations successfully capture the seasonal cycle, neither configuration does so, or only one out of the two model configurations achieves it.

The seasonal cycles at most surface stations are well captured by both configurations, with regards to both phase and amplitude, as illustrated in Fig. 6. Some stations exhibiting more complex and higher frequency patterns of CO_2 concentrations variation throughout seasons have a lower correlation coefficient. This pattern is observed for both configurations. However, almost all stations that are adequately modeled by the REG configuration with regards to seasonal cycles (correlation coefficient higher than 0.8) are equally well represented in the ICO configuration, as shown in Fig. 7 (a). Out of the 107 stations analyzed, only 12

318   stations did not exceed a correlation of 0.8 with the REG configuration, and 11 with the ICO configuration. Additionally, no

319   station exhibited satisfactory performance with REG but not with ICO, while the opposite was true for one station. The

320   amplitude of the seasonal cycle is also well captured for almost all stations, as shown in Fig. 7 (b).
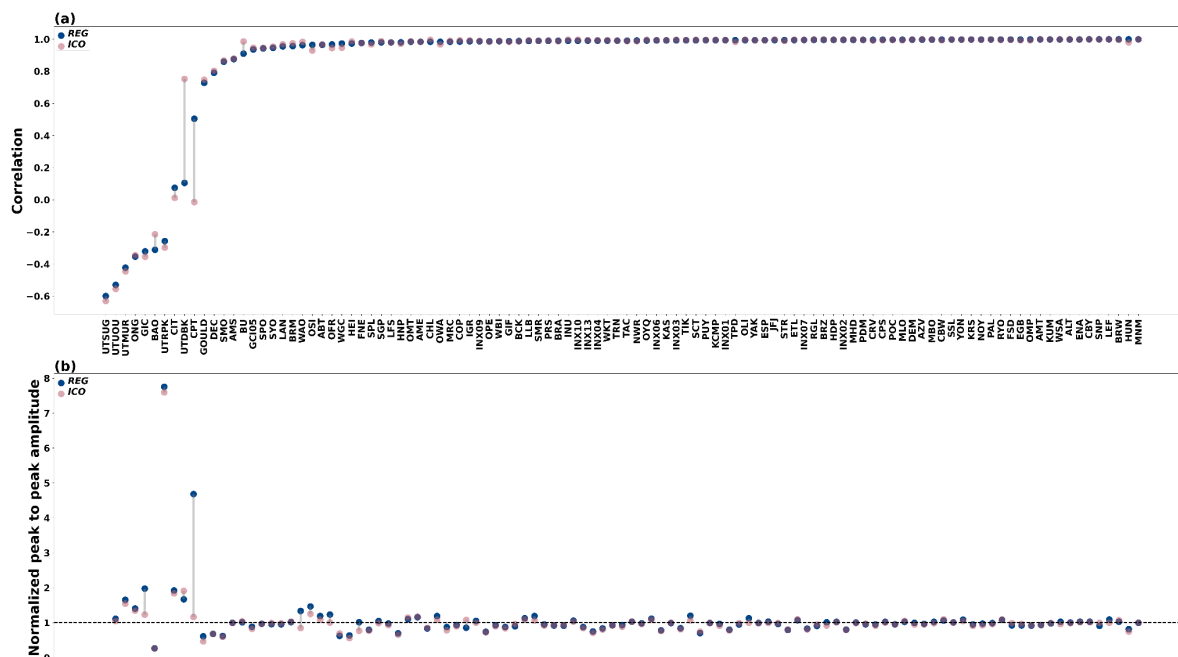
321

322   **Figure 7: Pearson correlation coefficient (a) and normalized standard deviation (b) of the seasonal cycle for all surface stations studied**
323   **averaged over the period 1980-2020, with blue circles for REG and red circles for ICO, the gray line is the difference between the two.**
324   **The stations are ordered on the abscissa by increasing correlation coefficient for REG.**

325   **3.4.2 Synoptic variability**

326
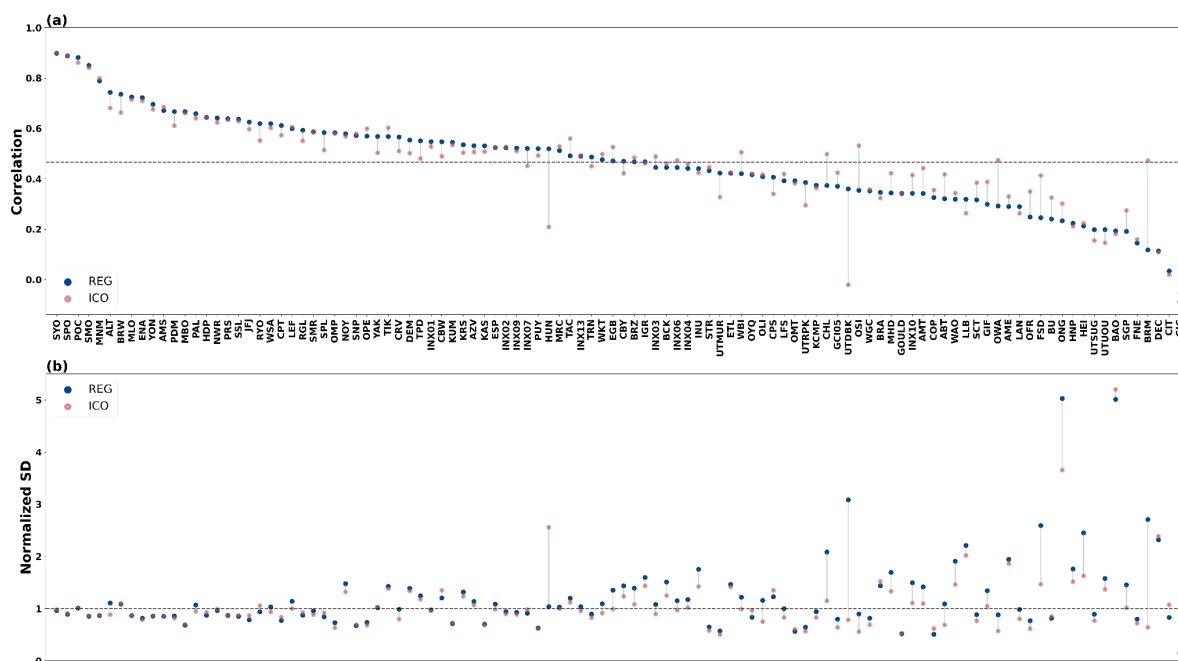
Figure 8: Pearson correlation (a) and normalized standard deviation (b) of the daily average residue between our modeled and measured CO₂ concentrations at the surface stations described in section 2.5 for the period 1980-2020. The model output from the REG and ICO configurations are in blue and red respectively.

To study the synoptic variability modeled by our two model configurations, we look at the correlation and the normalized standard deviation (NSD) of the daily averaged residue of our seasonal analysis for each surface station. This gives us information on the accuracy of our simulation for higher frequency than the seasonal cycles. Both configurations have correlation coefficients over 0.57 for 25% of all stations and a mean value of 0.47 for REG and ICO. The ICO configuration has a lower mean NSD of 1.06 compared to the one of REG of 1.20. And stations that offer a good correlation also tend to exhibit a better spread of the synoptic variability characterized by the NSD. These results are in line with what can be expected of a simulation at these resolutions as shown in Agustí-Panareda et al. (2019).

3.5 Vertical profiles of CO₂ concentrations

3.5.1 Troposphere
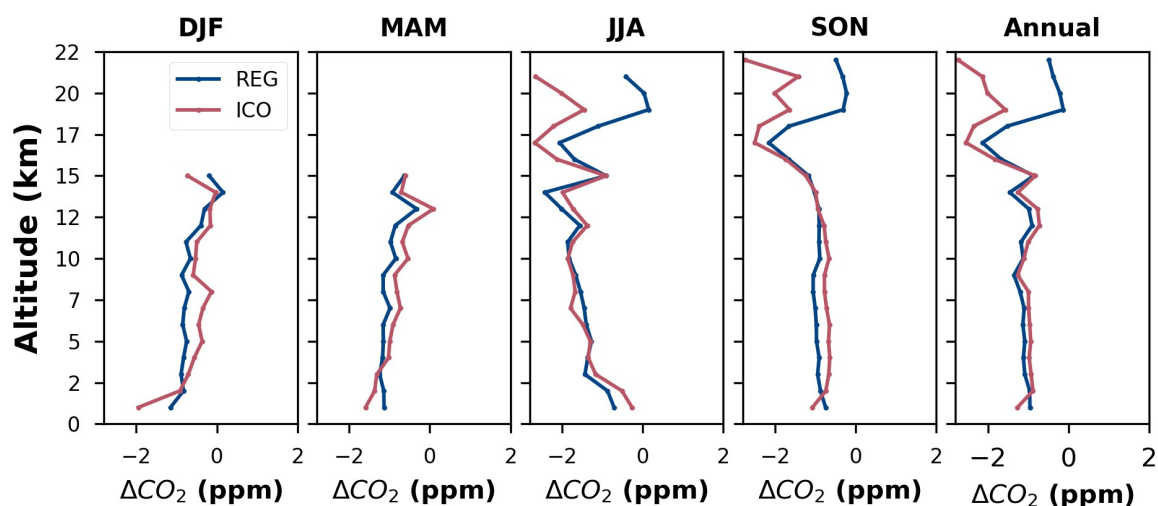
Figure 9: Seasonal and annual means of the difference in CO₂ vertical profile between the two model configurations of the model and aircraft measurements. The data has been binned into 1 km altitude bins for each season of the 1980-2020 period, then averaged per hour, and finally averaged across all aircraft sites and campaigns. The blue line represents the difference between REG and the measurements, while the red line represents the difference between ICO and the measurements.

In the troposphere, we studied CO₂ vertical profiles using various aircraft measurements described in section 2.4.2. Figure 9 shows the differences between the simulated and observed values for our two model configurations, REG and ICO. Only a small number of aircraft campaigns reach high altitudes above 15 km and not all seasons are covered. Both configurations show very similar vertical profiles up to 15 km altitude, before diverging above. Both configurations show a general negative bias compared to measurements. The variations in vertical gradients are almost identical for all altitudes, but the extent of the differences between model's output and measurements differ at high altitudes. REG has much greater variations in CO₂ concentrations while ICO has an increased negative bias at high altitudes. This is similar to the results in the next section 3.5.2.

3.5.2 Low stratosphere

We utilized data from AirCore flights to compare the CO_2 mixing ratios of our model with observed data and obtain vertical profiles extending to the low stratosphere, in order to investigate the potential effects of the change in dynamics on vertical mixing within a column. However, since these measurements were only conducted in latitudes higher than 30°N and lower than 30°S, information about vertical tracer transport in the tropics was not obtained. As shown in Fig. 10, both model configurations exhibit an excess of CO_2 concentrations around the 12.5 km range. However, the REG configuration has an additional peak in CO_2 concentrations at 20 km, followed by a gradient change and a subsequent decrease in concentration at higher altitudes. In contrast, the ICO configuration does not display the same peak at 20 km, but a similar gradient change is observed above this altitude. This finding suggests that tracer vertical transport is inadequate between the low and high stratosphere at these latitudes, and CO_2 accumulates at lower levels than expected for the REG configuration. While the ICO configuration employs the same van Leer vertical transport scheme, differences in the vertical temperature profiles (see Fig. 2 and Fig. 3) discussed in section 3.4 could explain the disparity in the vertical profile at the stratosphere. The attribution of this systematic error to a particular process is complicated by the high potential collection altitude determination error of AirCore measurements, which can be on the order of a kilometer in the stratosphere as discussed briefly in section 2.3 (Wagenhäuser et al., 2021). The previously discussed conclusions however are independently verified by the aircraft measurements that do not suffer from the altitude determination error and show similar differences in CO_2 concentrations at 20 km (Fig. 9).

368
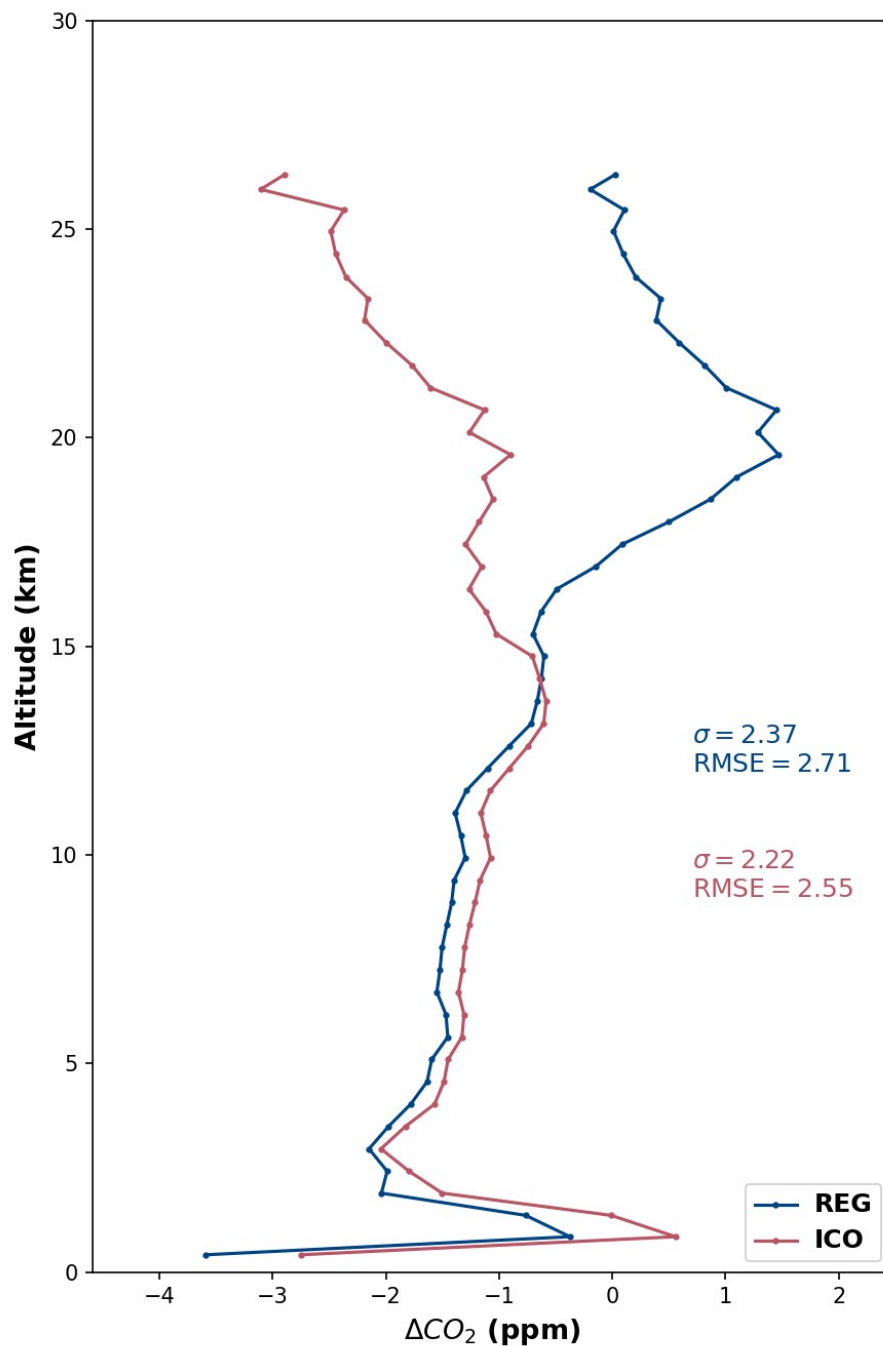
Figure 10: Difference in CO₂ mixing ratio vertical profile between the two model configurations of the model and AirCore measurements. The blue line represents the difference between the REG model output and measurements, while the red line indicates the difference between the ICO model output and measurements. The fitted lines were generated by averaging the data over 50 altitude bins.

4 Conclusion

As demonstrated in the previous section's results, the configuration ICO based on the new dynamical core Dynamico, using an unstructured grid is just as effective as the reference configuration that used a structured latitude-longitude grid for modeling atmospheric CO_2 transport when the dynamics was nudged to horizontal winds of an ERA5 reanalysis. Both configurations accurately capture the seasonal variations in CO_2 concentrations at most surface stations, and while the ICO configuration did not better capture more complex seasonal patterns, it did not worsen it either. A low percentage of station's seasonal cycles are properly captured by only one of the two model configurations. The annual gradient between stations exhibit slightly higher overall bias with ICO than with REG, but ICO has a smaller dispersion compared to observations. Regarding synoptic variability, the ICO configuration generally exhibits a lower correlation but a smaller standard deviation in comparison to observations. Nevertheless, both configurations provide an inadequate modeling of synoptic variability, as the local high-frequency emissions are poorly constrained.

Additionally, both configurations offer comparable vertical CO_2 concentration profiles and exhibit the same bias in the lower stratosphere relative to observational data. Temperature profiles in the tropopause and stratosphere seem to indicate that gravity waves still need to be tuned in the new ICO configuration (Lott et al., 2005). Their impact on atmospheric transport of CO_2 at lower altitudes has not been specifically evaluated but is expected to be minimal given the small differences shown between the two model configurations. Tuning of the climatology of the LMDZ - Dynamico coupling in general is still an ongoing process.

The new ICO configuration offers new opportunities in terms of development. Its use of fewer cells per level for a comparable resolution at the equator results in faster computation times of around 20% in our tests and easier-to-store outputs thanks to their smaller size on disk. Unlike regular latitude-longitude grids, ICO does not require a polar filter, whereas these filters generally parallelize badly, on both CPU and GPU. It gives a more homogeneous grid compared to the higher resolution at the poles of a regular latitude-longitude grid which is not always needed for modelisation at a global scale.

While running, REG and ICO can archive specific meteorological variables like air mass fluxes which can then be read by an offline version of the model dedicated to tracer transport. This economical transport model forms the basis of the inversion system of Chevallier et al. (2005) to generate the CO_2 and N_2O inversion products of the Copernicus Atmosphere Monitoring Service of the European Commission (CAMS service, https://atmosphere.copernicus.eu/ghg-services). Our next task is the implementation of Dynamico in this offline model in order to prepare future resolution increases, while damping the induced increase of the code time-to-solution.

Code and data availability

The source code for the REG and ICO configurations is freely available online via the following address: https://forge.ipsl.jussieu.fr/igcmg/browser/CONFIG/publications/ICOLMDZORINCA_CO2_Transport_GMD_2023

under the CeCILL v2 Free Software License (http://www.cecill.info/index.en.html, last access: 11 September 2023, CECILL, 2020). The exact version of the model used to produce the results used in this paper is archived on Zenodo, as are input data and scripts to run the model and produce the plots for all the simulations presented in this paper (Lloret et al., 2023).

Author contributions

ZL designed, ran and analyzed the simulations and prepared the paper under direction and advice of FC. AC contributed to the development and preparation of the simulations. MR was also involved in the development of the simulations. YM supported the development of the model. All authors contributed to the text.

Disclaimer

The authors declare that they have no conflict of interest.

Acknowledgements

This work was granted access to the HPC resources of TGCC under the allocation A0130102201 made by GENCI. It was funded by the Copernicus Atmosphere Monitoring Service, implemented by ECMWF on behalf of the European Commission (Grant: CAMS2 55). We thank Olivier Boucher for fruitful discussions on vertical temperature profiles and the LMDZ model, and Sakina Takache for discussions on Dynamico. We also thank Julien Derouillat for his help in the implementation of XIOS for our application. We also gratefully acknowledge the many people who contributed atmospheric observations (aircraft, AirCore and surface air sample measurements). Measurements at Jungfraujoch were supported by ICOS Switzerland, which is funded by the Swiss National Science Foundation, in-house contributions and the State Secretariat for Education, Research and Innovation. We thank Kathryn McKain for her comments and suggestions on the best way to describe aircraft and AirCore data.

References

Agustí-Panareda, A., Diamantakis, M., Massart, S., Chevallier, F., Muñoz-Sabater, J., Barré, J., Curcoll, R., Engelen, R., Langerock, B., Law, R. M., Loh, Z., Morguí, J. A., Parrington, M., Peuch, V.-H., Ramonet, M., Roehl, C., Vermeulen, A. T., Warneke, T., and Wunch, D.: Modelling CO_2 weather – why horizontal resolution matters, Atmospheric Chemistry and Physics, 19, 7347–7376, https://doi.org/10.5194/acp-19-7347-2019, 2019.

Agustí-Panareda, A., McNorton, J., Balsamo, G., Baier, B. C., Bousserez, N., Boussetta, S., Brunner, D., Chevallier, F., Choulga, M., Diamantakis, M., Engelen, R., Flemming, J., Granier, C., Guevara, M., Denier van der Gon, H., Elguindi, N., Haussaire, J.-M., Jung, M., Janssens-Maenhout, G., Kivi, R., Massart, S., Papale, D., Parrington, M., Razinger, M., Sweeney, C., Vermeulen, A., and Walther, S.: Global nature run data with realistic high-resolution carbon weather for the year of the Paris Agreement, Sci Data, 9, 160, https://doi.org/10.1038/s41597-022-01228-2, 2022.

Basu, S., Baker, D. F., Chevallier, F., Patra, P. K., Liu, J., and Miller, J. B.: The impact of transport model differences on CO_2 surface flux estimates from OCO-2 retrievals of column average CO_2, Atmospheric Chemistry and Physics, 18, 7189–7215, https://doi.org/10.5194/acp-18-7189-2018, 2018.

Cadule, P., Friedlingstein, P., Bopp, L., Sitch, S., Jones, C. D., Ciais, P., Piao, S. L., and Peylin, P.: Benchmarking coupled climate-carbon models against long-term atmospheric CO2 measurements, Global Biogeochemical Cycles, 24, https://doi.org/10.1029/2009GB003556, 2010.

CeCILL: CeCILL and Free Software, http://www.cecill.info/index.en.html (last access: 3 July 2023), 2020.

Chevallier, F., M. Fisher, P. Peylin, S. Serrar, P. Bousquet, F.-M. Bréon, A. Chédin, and P. Ciais, 2005: Inferring CO2 sources and sinks from satellite observations: method and application to TOVS data. J. Geophys. Res., 110, D24309, doi:10.1029/2005JD006390.

Chevallier, F., Lloret, Z., Cozic, A., Takache, S., and Remaud, M.: Toward High-Resolution Global Atmospheric Inverse Modeling Using Graphics Accelerators, Geophysical Research Letters, 50, e2022GL102135, https://doi.org/10.1029/2022GL102135, 2023.

444   Ciais, P., Dolman, A. J., Bombelli, A., Duren, R., Peregon, A., Rayner, P. J., Miller, C., Gobron, N., Kinderman, G., Marland,
445   G., Gruber, N., Chevallier, F., Andres, R. J., Balsamo, G., Bopp, L., Bréon, F.-M., Broquet, G., Dargaville, R., Battin, T. J.,
446   Borges, A., Bovensmann, H., Buchwitz, M., Butler, J., Canadell, J. G., Cook, R. B., DeFries, R., Engelen, R., Gurney, K. R.,
447   Heinze, C., Heimann, M., Held, A., Henry, M., Law, B., Luyssaert, S., Miller, J., Moriyama, T., Moulin, C., Myneni, R. B.,
448   Nussli, C., Obersteiner, M., Ojima, D., Pan, Y., Paris, J.-D., Piao, S. L., Poulter, B., Plummer, S., Quegan, S., Raymond, P.,
449   Reichstein, M., Rivier, L., Sabine, C., Schimel, D., Tarasova, O., Valentini, R., Wang, R., van der Werf, G., Wickland, D.,
450   Williams, M., and Zehner, C.: Current systematic carbon-cycle observations and the need for implementing a policy-relevant
451   carbon observing system, Biogeosciences, 11, 3547–3602, https://doi.org/10.5194/bg-11-3547-2014, 2014.

452   Crotwell, A., Lee, H., Steinbacher, M., Eds.: "20th WMO/IAEA Meeting on Carbon Dioxide, Other Greenhouse Gases and
453   Related Measurement Techniques (GGMT-2019)," GAW REPORT No. 255 (World Meteorological Organization, 2020);
454   https://library.wmo.int/doc_num.php?explnum_id=10353, 2020.

455   Dubey, S., Dubos, T., Hourdin, F., and Upadhyaya, H. C.: On the inter-comparison of two tracer transport schemes on
456   icosahedral grids, Applied Mathematical Modelling, 39, 4828–4847, https://doi.org/10.1016/j.apm.2015.04.015, 2015.

457   Dubos, T. and Tort, M.: Equations of Atmospheric Motion in Non-Eulerian Vertical Coordinates: Vector-Invariant Form and
458   Quasi-Hamiltonian Formulation, Monthly Weather Review, 142, 3860–3880, https://doi.org/10.1175/MWR-D-14-00069.1,
459   2014.

460   Dubos, T., Dubey, S., Tort, M., Mittal, R., Meurdesoif, Y., and Hourdin, F.: DYNAMICO-1.0, an icosahedral hydrostatic
461   dynamical core designed for consistency and versatility, Geosci. Model Dev., 8, 3131–3150, https://doi.org/10.5194/gmd-8-
462   3131-2015, 2015.

463   Ducoudré, N. I., Laval, K., and Perrier, A.: SECHIBA, a New Set of Parameterizations of the Hydrologic Exchanges at the Land-
464   Atmosphere Interface within the LMD Atmospheric General Circulation Model, J. Climate, 6, 248–273,
465   https://doi.org/10.1175/1520-0442(1993)006<0248:SANSOP>2.0.CO;2, 1993.

466   Emanuel, K. A.: A Scheme for Representing Cumulus Convection in Large-Scale Models, Journal of the Atmospheric Sciences,
467   48, 2313–2329, https://doi.org/10.1175/1520-0469(1991)048<2313:ASFRCC>2.0.CO;2, 1991.

468   Evangeliou, N., Balkanski, Y., Cozic, A., and Møller, A. P.: Simulations of the transport and deposition of
469   ¹³⁷Cs over Europe after the Chernobyl Nuclear Power Plant accident: influence of varying emission-
470   altitude and model horizontal and vertical resolution, Atmos. Chem. Phys., 13, 7183–7198, https://doi.org/10.5194/acp-13-7183-
471   2013, 2013.

472   Folberth, G. A., Hauglustaine, D. A., Lathière, J., and Brocheton, F.: Interactive chemistry in the Laboratoire de Météorologie
473   Dynamique general circulation model: model description and impact analysis of biogenic hydrocarbons on tropospheric
474   chemistry, Atmospheric Chemistry and Physics, 6, 2273–2319, https://doi.org/10.5194/acp-6-2273-2006, 2006.

475   Fouquart, Y. and Bonnel, B.: Computations of solar heating of the earth's atmosphere: A new parameterization, Beitr. Phys.
476   Atmos., 53, 35–62, 1980.

477   Giorgetta, M. A., Brokopf, R., Crueger, T., Esch, M., Fiedler, S., Helmert, J., Hohenegger, C., Kornblueh, L., Köhler, M.,
478   Manzini, E., Mauritsen, T., Nam, C., Raddatz, T., Rast, S., Reinert, D., Sakradzija, M., Schmidt, H., Schneck, R., Schnur, R.,
479   Silvers, L., Wan, H., Zängl, G., and Stevens, B.: ICON-A, the Atmosphere Component of the ICON Earth System Model: I.
480   Model Description, Journal of Advances in Modeling Earth Systems, 10, 1613–1637, https://doi.org/10.1029/2017MS001242,
481   2018.

482   Grandpeix, J.-Y., Phillips, V., and Tailleux, R.: Improved mixing representation in Emanuel's convection scheme, Q. J. R.
483   Meteorol. Soc., 130, 3207–3222, https://doi.org/10.1256/qj.03.144, 2004.

484   Hazan, L., Tarniewicz, J., Ramonet, M., Laurent, O., and Abbaris, A.: Automatic processing of atmospheric CO2 and CH4 mole
485   fractions at the ICOS Atmosphere Thematic Centre, Atmospheric Measurement Techniques, 9, 4719–4736,
486   https://doi.org/10.5194/amt-9-4719-2016, 2016.

487   Herrington, A. R., Lauritzen, P. H., Lofverstrom, M., Lipscomb, W. H., Gettelman, A., and Taylor, M. A.: Impact of grids and
488   dynamical cores in CESM2.2 on the surface mass balance of the Greenland Ice Sheet, Journal of Advances in Modeling Earth
489   Systems, n/a, e2022MS003192, https://doi.org/10.1029/2022MS003192, n.d.

490   Hersbach, H., Bell, B., Berrisford, P., Hirahara, S., Horányi, A., Muñoz-Sabater, J., Nicolas, J., Peubey, C., Radu, R., Schepers,
491   D., Simmons, A., Soci, C., Abdalla, S., Abellan, X., Balsamo, G., Bechtold, P., Biavati, G., Bidlot, J., Bonavita, M., De Chiara,
492   G., Dahlgren, P., Dee, D., Diamantakis, M., Dragani, R., Flemming, J., Forbes, R., Fuentes, M., Geer, A., Haimberger, L., Healy,
493   S., Hogan, R. J., Hólm, E., Janisková, M., Keeley, S., Laloyaux, P., Lopez, P., Lupu, C., Radnoti, G., de Rosnay, P., Rozum, I.,
494   Vamborg, F., Villaume, S., and Thépaut, J.-N.: The ERA5 global reanalysis, Quarterly Journal of the Royal Meteorological
495   Society, 146, 1999–2049, https://doi.org/10.1002/qj.3803, 2020.

496   Hourdin, F., Musat, I., Bony, S., Braconnot, P., Codron, F., Dufresne, J.-L., Fairhead, L., Filiberti, M.-A., Friedlingstein, P.,
497   Grandpeix, J.-Y., Krinner, G., LeVan, P., Li, Z.-X., and Lott, F.: The LMDZ4 general circulation model: climate performance
498   and sensitivity to parametrized physics with emphasis on tropical convection, Clim Dyn, 27, 787–813,
499   https://doi.org/10.1007/s00382-006-0158-0, 2006.

500   Hourdin, F., Grandpeix, J.-Y., Rio, C., Bony, S., Jam, A., Cheruy, F., Rochetin, N., Fairhead, L., Idelkadi, A., Musat, I.,
501   Dufresne, J.-L., Lahellec, A., Lefebvre, M.-P., and Roehrig, R.: LMDZ5B: the atmospheric component of the IPSL climate
502   model with revisited parameterizations for clouds and convection, Clim Dyn, 40, 2193–2222, https://doi.org/10.1007/s00382-
503   012-1343-y, 2013.

504   Hourdin, F., Rio, C., Grandpeix, J.-Y., Madeleine, J.-B., Cheruy, F., Rochetin, N., Jam, A., Musat, I., Idelkadi, A., Fairhead, L.,
505   Foujols, M.-A., Mellul, L., Traore, A.-K., Dufresne, J.-L., Boucher, O., Lefebvre, M.-P., Millour, E., Vignon, E., Jouhaud, J.,
506   Diallo, F. B., Lott, F., Gastineau, G., Caubel, A., Meurdesoif, Y., and Ghattas, J.: LMDZ6A: The Atmospheric Component of the
507   IPSL Climate Model With Improved and Better Tuned Physics, Journal of Advances in Modeling Earth Systems, 12,
508   e2019MS001892, https://doi.org/10.1029/2019MS001892, 2020.

509   Houweling, S., Aben, I., Breon, F.-M., Chevallier, F., Deutscher, N., Engelen, R., Gerbig, C., Griffith, D., Hungershoefer, K.,
510   Macatangay, R., Marshall, J., Notholt, J., Peters, W., and Serrar, S.: The importance of transport model uncertainties for the
511   estimation of CO2 sources and sinks using satellite measurements, Atmos. Chem. Phys., 10, 9981–9992,
512   https://doi.org/10.5194/acp-10-9981-2010, 2010.

513   Kenneth N. Schuldt, John Mund, Ingrid T. Luijkx, Tuula Aalto, James B. Abshire, Ken Aikin, Arlyn Andrews, Shuji Aoki,
514   Francesco Apadula, Bianca Baier, Peter Bakwin, Jakub Bartyzel, Gilles Bentz, Peter Bergamaschi, Andreas Beyersdorf, Tobias
515   Biermann, Sebastien C. Biraud, Harald Boenisch, David Bowling, Gordon Brailsford, Willi A. Brand, Huilin Chen, Gao Chen,
516   Lukasz Chmura, Shane Clark, Sites Climadat, Aurelie Colomb, Roisin Commane, Sébastien Conil, Cedric Couret, Adam Cox,
517   Paolo Cristofanelli, Emilio Cuevas, Roger Curcoll, Bruce Daube, Kenneth Davis, Martine De Mazière, Stephan De Wekker,
518   Julian Della Coletta, Marc Delmotte, Joshua P. DiGangi, Ed Dlugokencky, James W. Elkins, Lukas Emmenegger, Shuangxi
519   Fang, Marc L. Fischer, Grant Forster, Arnoud Frumau, Michal Galkowski, Luciana V. Gatti, Torsten Gehrlein, Christoph Gerbig,
520   Francois Gheusi, Emanuel Gloor, Vanessa Gomez-Trueba, Daisuke Goto, Tim Griffis, Samuel Hammer, Chad Hanson, László
521   Haszpra, Juha Hatakka, Martin Heimann, Michal Heliasz, Daniela Heltai, Arjan Hensen, Ove Hermanssen, Eric Hintsa, Antje
522   Hoheisel, Jutta Holst, Viktor Ivakhov, Dan Jaffe, Armin Jordan, Warren Joubert, Anna Karion, Stephan R. Kawa, Victor Kazan,
523   Ralph Keeling, Petri Keronen, Jooil Kim, Tobias Kneuer, Pasi Kolari, Katerina Kominkova, Eric Kort, Elena Kozlova, Paul

524 Krummel, Dagmar Kubistin, Casper Labuschagne, David H. Lam, Xin Lan, Ray Langenfelds, Olivier Laurent, Tuomas Laurila,
525 Thomas Lauvaux, Jost Lavric, Bev Law, Olivia S. Lee, John Lee, Irene Lehner, Kari Lehtinen, Reimo Leppert, Ari Leskinen,
526 Markus Leuenberger, Ingeborg Levin, Janne Levula, John Lin, Matthias Lindauer, Zoe Loh, Morgan Lopez, Chris R. Lunder,
527 Toshinobu Machida, Ivan Mammarella, Giovanni Manca, Alistair Manning, Andrew Manning, Michal V. Marek, Melissa Y.
528 Martin, Giordane A. Martins, Hidekazu Matsueda, Kathryn McKain, Harro Meijer, Frank Meinhardt, Lynne Merchant, N.
529 Mihalopoulos, Natasha Miles, John B. Miller, Charles E. Miller, Logan Mitchell, Stephen Montzka, Fred Moore, Heiko
530 Moossen, Eric Morgan, Josep-Anton Morgui, Shinji Morimoto, Bill Munger, David Munro, Cathrine L. Myhre, Meelis Mölder,
531 Jennifer Müller-Williams, Jaroslaw Necki, Sally Newman, Sylvia Nichol, Yosuke Niwa, Simon O\'Doherty, Florian Obersteiner,
532 Bill Paplawsky, Jeff Peischl, Olli Peltola, Salvatore Piacentino, Jean M. Pichon, Steve Piper, Joseph Pitt, Christian Plass-
533 Duelmer, Stephen M. Platt, Steve Prinzivalli, Michel Ramonet, Ramon Ramos, Enrique Reyes-Sanchez, Scott Richardson, Haris
534 Riris, Pedro P. Rivas, Michael Rothe, Thomas Ryerson, Kazuyuki Saito, Maryann Sargent, Motoki Sasakawa, Bert Scheeren,
535 Martina Schmidt, Tanja Schuck, Marcus Schumacher, Thomas Seifert, Mahesh K. Sha, Paul Shepson, Michael Shook,
536 Christopher D. Sloop, Paul Smith, Martin Steinbacher, Britton Stephens, Colm Sweeney, Lise L. Sørensen, Pieter Tans, Kirk
537 Thoning, Helder Timas, Margaret Torn, Pamela Trisolino, Jocelyn Turnbull, Kjetil Tørseth, Alex Vermeulen, Brian Viner,
538 Gabriela Vitkova, Stephen Walker, Andrew Watson, Ray Weiss, Steve Wofsy, Justin Worsey, Doug Worthy, Dickon Young,
539 Sönke Zaehle, Andreas Zahn, Miroslaw Zimnoch, Rodrigo A. de Souza, Alcide G. di Sarra, Danielle van Dinther, Pim van den
540 Bulk; Multi-laboratory compilation of atmospheric carbon dioxide data for the period 1957-2021;
541 obspack_co2_1_GLOBALVIEWplus_v8.0_2022-08-27; NOAA Earth System Research Laboratory, Global Monitoring
542 Laboratory. http://doi.org/10.25925/20220808.

543 Krinner, G., Viovy, N., de Noblet-Ducoudré, N., Ogée, J., Polcher, J., Friedlingstein, P., Ciais, P., Sitch, S., and Prentice, I. C.: A
544 dynamic global vegetation model for studies of the coupled atmosphere-biosphere system, Global Biogeochemical Cycles, 19,
545 https://doi.org/10.1029/2003GB002199, 2005.

546 Lauvaux, T., Pannekoucke, O., Sarrat, C., Chevallier, F., Ciais, P., Noilhan, J., and Rayner, P. J.: Structure of the transport
547 uncertainty in mesoscale inversions of CO_2 sources and sinks using ensemble model simulations, Biogeosciences, 6, 1089–1102,
548 https://doi.org/10.5194/bg-6-1089-2009, 2009.

549 Lin, X., Ciais, P., Bousquet, P., Ramonet, M., Yin, Y., Balkanski, Y., Cozic, A., Delmotte, M., Evangeliou, N., Indira, N. K.,
550 Locatelli, R., Peng, S., Piao, S., Saunois, M., Swathi, P. S., Wang, R., Yver-Kwok, C., Tiwari, Y. K., and Zhou, L.: Simulating
551 CH_4 and CO_2 over South and East Asia using the zoomed chemistry transport model LMDz-INCA, Atmospheric Chemistry and
552 Physics, 18, 9475–9497, https://doi.org/10.5194/acp-18-9475-2018, 2018.

553 Lloret, Z., Cozic, A., Chevallier, F., Remaud, M., & Meurdesoif, Y.: ICOLMDZORINCA CO2 Transport GMD 2023. Zenodo.
554 https://doi.org/10.5281/zenodo.10019679, 2023.

555 Lott, F., Fairhead, L., Hourdin, F., and Levan, P.: The stratospheric version of LMDz: dynamical climatologies, arctic oscillation,
556 and impact on the surface climate, Clim Dyn, 25, 851–868, https://doi.org/10.1007/s00382-005-0064-x, 2005.

557 Mellor, G. L. and Yamada, T.: A Hierarchy of Turbulence Closure Models for Planetary Boundary Layers, Journal of the
558 Atmospheric Sciences, 31, 1791–1806, https://doi.org/10.1175/1520-0469(1974)031<1791:AHOTCM>2.0.CO;2, 1974.

559 Mlawer, E. J., Taubman, S. J., Brown, P. D., Iacono, M. J., and Clough, S. A.: Radiative transfer for inhomogeneous
560 atmospheres: RRTM, a validated correlated-k model for the longwave, Journal of Geophysical Research: Atmospheres, 102,
561 16663–16682, https://doi.org/10.1029/97JD00237, 1997.

562 Niwa, Y., Tomita, H., Satoh, M., Imasu, R., Sawa, Y., Tsuboi, K., Matsueda, H., Machida, T., Sasakawa, M., Belan, B., and
563 Saigusa, N.: A 4D-Var inversion system based on the icosahedral grid model (NICAM-TM 4D-Var v1.0) – Part 1: Offline
564 forward and adjoint transport models, Geosci. Model Dev., 10, 1157–1174, https://doi.org/10.5194/gmd-10-1157-2017, 2017.

565 Remaud, M., Chevallier, F., Cozic, A., Lin, X., and Bousquet, P.: On the impact of recent developments of the LMDz
566 atmospheric general circulation model on the simulation of CO2 transport, Geosci. Model Dev., 25, 2018.

567 Rio, C., Hourdin, F., Grandpeix, J.-Y., and Lafore, J.-P.: Shifting the diurnal cycle of parameterized deep convection over land,
568 Geophysical Research Letters, 36, https://doi.org/10.1029/2008GL036779, 2009.

569 Rochetin, N., Grandpeix, J.-Y., Rio, C., and Couvreux, F.: Deep Convection Triggering by Boundary Layer Thermals. Part II:
570 Stochastic Triggering Parameterization for the LMDZ GCM, Journal of the Atmospheric Sciences, 71, 515–538,
571 https://doi.org/10.1175/JAS-D-12-0337.1, 2014.

572 Sakaguchi, K., Harrop, B. E., Leung, L. R., Jang, J., Gettelman, A., Zarzycki, C. M., Lin, G., Zhang, K., and Skamarock, W. C.:
573 The CAM-MPAS model simulations for the HighResMIP experiments, 2020, A090-0014, 2020.

574 Sepulchre, P., Caubel, A., Ladant, J.-B., Bopp, L., Boucher, O., Braconnot, P., Brockmann, P., Cozic, A., Donnadieu, Y.,
575 Dufresne, J.-L., Estella-Perez, V., Ethé, C., Fluteau, F., Foujols, M.-A., Gastineau, G., Ghattas, J., Hauglustaine, D., Hourdin, F.,
576 Kageyama, M., Khodri, M., Marti, O., Meurdesoif, Y., Mignot, J., Sarr, A.-C., Servonnat, J., Swingedouw, D., Szopa, S., and
577 Tardif, D.: IPSL-CM5A2 – an Earth system model designed for multi-millennial climate simulations, Geoscientific Model
578 Development, 13, 3011–3053, https://doi.org/10.5194/gmd-13-3011-2020, 2020.

579 Shepherd, T. G., Semeniuk, K., and Koshyk, J. N.: Sponge layer feedbacks in middle-atmosphere models, Journal of
580 Geophysical Research: Atmospheres, 101, 23447–23464, https://doi.org/10.1029/96JD01994, 1996.

581 Staniforth, A. and Thuburn, J.: Horizontal grids for global weather and climate prediction models: a review, Quarterly Journal of
582 the Royal Meteorological Society, 138, 1–26, https://doi.org/10.1002/qj.958, 2012.

583 Tort, M., Dubos, T., Bouchut, F., and Zeitlin, V.: Consistent shallow-water equations on the rotating sphere with complete
584 Coriolis force and topography, Journal of Fluid Mechanics, 748, 789–821, https://doi.org/10.1017/jfm.2014.172, 2014.

585 Ullrich, P. A., Jablonowski, C., Kent, J., Lauritzen, P. H., Nair, R., Reed, K. A., Zarzycki, C. M., Hall, D. M., Dazlich, D.,
586 Heikes, R., Konor, C., Randall, D., Dubos, T., Meurdesoif, Y., Chen, X., Harris, L., Kühnlein, C., Lee, V., Qaddouri, A., Girard,
587 C., Giorgetta, M., Reinert, D., Klemp, J., Park, S.-H., Skamarock, W., Miura, H., Ohno, T., Yoshida, R., Walko, R., Reinecke,
588 A., and Viner, K.: DCMIP2016: a review of non-hydrostatic dynamical core design and intercomparison of participating models,
589 Geoscientific Model Development, 10, 4477–4509, https://doi.org/10.5194/gmd-10-4477-2017, 2017.

590 Van Leer, B.: Towards the ultimate conservative difference scheme. IV. A new approach to numerical convection, Journal of
591 Computational Physics, 23, 276–299, https://doi.org/10.1016/0021-9991(77)90095-X, 1977.

592 Wagenhäuser, T., Engel, A., and Sitals, R.: Testing the altitude attribution and vertical resolution of AirCore measurements with
593 a new spiking method, Atmospheric Measurement Techniques, 14, 3923–3934, https://doi.org/10.5194/amt-14-3923-2021, 2021.